Supplemental Material for Rayleigh Anomaly Induced Phase Gradients in Finite Nanoparticle Chains

Lior Michaeli[1-4,*], Ofer Doron[1-3], Yakir Hadad[1], Haim Suchowski[2,3], Tal Ellenbogen[1,3]

[1] *Department of Physical Electronics, Faculty of Engineering, Tel-Aviv University, Tel-Aviv 6779801, Israel*
[2] *Raymond and Beverly Sackler School of Physics & Astronomy, Tel-Aviv University, Tel-Aviv 6779801, Israel*
[3] *Center for Light-Matter Interaction, Tel-Aviv University, Tel-Aviv 6779801, Israel*
[4] Currently at: *Thomas J. Watson Laboratories of Applied Physics, California Institute of Technology, Pasadena, California, 91125, USA*

In this document we provide a support to the study of the RA induced phase gradients presented in the main text. The document is organized as follow: In Section 1 we derive an analytical condition for the model accuracy. In section 2 we show a numerical verification of the model accuracy. In section 3 we plot the number of scattering paths as a function of the number of particles in the chain. In section 4 we give an example of a nanoparticle the supports the studied polarizability. In section 5 we show the studied wavelength dependent polarizability. In section 6 we plot the diffraction patterns of the studied chain. In section 7 we demonstrate the effect of RA induced phase gradients in longer chains. In section 8 we discuss how the phase gradients can be understood from the dependence of B_q on q. In section 9 we discuss how the already reported phenomenon of RA induced transparency can be understood by the developed framework. In section 10 we analyze the RA induced phase gradients with an established macroscopic theory. Finally, in section 11, we elaborate how we calculate the power of the diffracted beams.

1. Analytical Condition for the Model Accuracy

To analyze the accuracy of the model approximation, presented in Eq. (14) of the main text, we will rely on the theory of sensitivity analysis in linear systems[1]. For the linear system $\hat{A}p = E_{app}$, any perturbation of $\hat{A}$ to $\hat{A} + \Delta\hat{A}$ will result in a corresponding perturbation of the solution vector p:

$$\left(\hat{A} + \Delta\hat{A}\right)(p + \Delta p) = E_{app} \tag{S1}$$

Quantification of the solution's error is given by means of its norm[1]:

$$\frac{\|\Delta p\|}{\|p\|} \leq cond\left(\hat{A}\right)\frac{\left\|\Delta\hat{A}\right\|}{\left\|\hat{A}\right\|} \tag{S2}$$

Where $\|p\|$ denotes the norm of the vector p, $\|A\|$ and $\left\|\Delta\hat{A}\right\|$ denote the norm of the corresponding matrices, and $cond\left(\hat{A}\right)$ is the condition number of the matrix $\hat{A}$, which determines the sensitivity of the solution to small changes in the input data. To quantify the expression in Eq. (S2, we first write an exact expression to $\left\|\hat{A}\right\|$, then we derive an upper bound to $\left\|\Delta\hat{A}\right\|$. For that, we will use the definition of a maximum norm to the matrices: $\left\|\hat{A}\right\|_M = \max_{i,j}\left|A_{ij}\right|$. In addition, in order to simplify the derivation, we will account only for the radiative term in the green function g_q (Eq. (3)), and write $g_q = \frac{g_1}{q}$. This approximation is justified as long as near fields do not play an important role in the interaction between the particles.

Calculation of $\left\|\hat{A}\right\|$:
The magnitude of largest element of $\hat{A}$ is the value of the diagonal elements:

$$\|\widehat{A}\|_M = |A_{ii}|^2 = |\alpha_s|^{-2} \tag{S3}$$

Upper bound to $\left\|\Delta\hat{A}\right\|$:

To estimate $\left\|\Delta\hat{A}\right\|$ we first need to obtain $\Delta\hat{A}$. Using the definition $\Delta\hat{A} \equiv \hat{A}_{Model} - \hat{A}$, we can perform the explicit multiplication to find $\Delta\hat{A}$. For example, for $N = 4$ we get:

$$\Delta\hat{A} = -\alpha_s \begin{bmatrix} 0 & 0 & 0 & 0 \\ 0 & g_1^2 & g_1 g_2 & g_1 g_3 \\ 0 & g_1 g_2 & g_1^2 + g_2^2 & g_1 g_2 + g_2 g_3 \\ 0 & g_1 g_3 & g_1 g_2 + g_2 g_3 & g_1^2 + g_2^2 + g_3^2 \end{bmatrix} \approx -\alpha_s g_1^2 \begin{bmatrix} 0 & 0 & 0 & 0 \\ 0 & \frac{1}{1} & \frac{1}{1}\cdot\frac{1}{2} & \frac{1}{1}\cdot\frac{1}{3} \\ 0 & \frac{1}{1}\cdot\frac{1}{2} & \frac{1}{1^2}+\frac{1}{2^2} & \frac{1}{1}\cdot\frac{1}{2}+\frac{1}{2}\cdot\frac{1}{3} \\ 0 & \frac{1}{1}\cdot\frac{1}{3} & \frac{1}{1}\cdot\frac{1}{2}+\frac{1}{2}\cdot\frac{1}{3} & \frac{1}{1^2}+\frac{1}{2^2}+\frac{1}{3^2} \end{bmatrix}$$

The largest element is the last element on the diagonal:

$$\left\|\Delta\hat{A}\right\|_\infty = |\alpha_s|^2 |g_1|^4 \left|\sum_{i=1}^{N-1} \frac{1}{i^2}\right|^2 \leq |\alpha_s|^2 |g_1|^4 \frac{\pi^2}{6} \tag{S4}$$

Where in the last step we used $\lim_{N\to\infty} \sum_{i=1}^{N-1} \frac{1}{i^2} = \pi^2/6$ to write the upper bound.

Mathematical condition for the model validity:

Using Eqs. (S2), (S3) and (S5) we can now obtain the condition for the validity of the model by demanding $cond(A) \ll \frac{\|\hat{A}\|}{\|\Delta\hat{A}\|}$:

$$cond(A) \ll \frac{6}{\pi^2} \cdot \frac{1}{|\zeta|^4} \equiv C(\zeta) \tag{S5}$$

This condition was derived without accounting for the specific illumination field E_{app}, and therefore is true for any arbitrary illumination profile. We also note that this is a stringent condition, as we have taken a lower bound to $\left\|\hat{A}\right\|/\left\|\Delta\hat{A}\right\|$. The derived expression $C(\zeta)$ strongly diverges as $|\zeta|$ goes to zero, showing that for weakly interacting particles the model is exact. To estimate the validity of the model for larger $|\zeta|$ the condition number of the interaction matrix $\hat{A}$ should be evaluated. For all the parameters considered at the manuscript, the condition number calculated according to the maximum norm definition $cond(\hat{A}) = \left\|\hat{A}\right\|_M \left\|\hat{A}^{-1}\right\|_M$ is on the order of $cond(\hat{A}) \approx 1$. Figure FIG. S1 shows the dependence of $C(\zeta)$ on $|\zeta|$. As the curve of $C(\zeta)$ gets larger than one the model becomes more accurate.

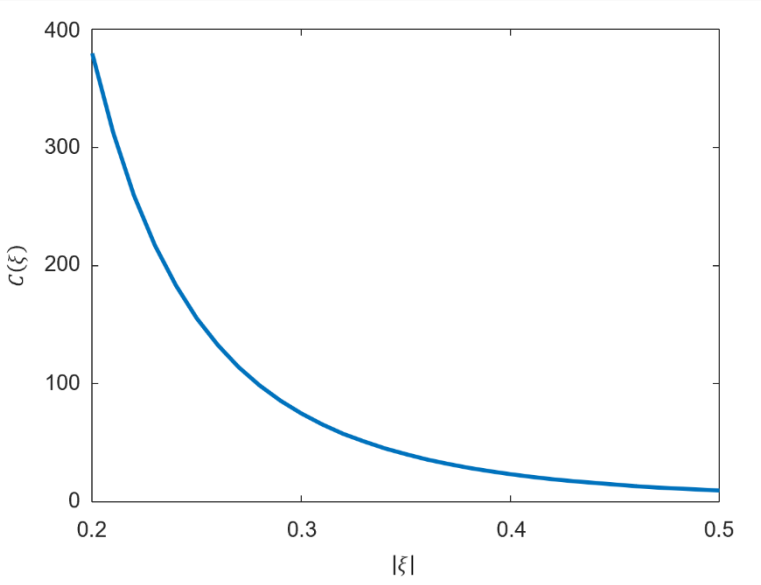

FIG. S1 The dependence of the model accuracy on $|\zeta|$. For accurate results the interaction matrix $\hat{A}$ should satisfy $cond(A) \ll C(\zeta)$.

2. Numerical Verification of the Model Accuracy

In FIG. S2(a) and FIG. S2(b), we directly examine the model assumption in Eq. (14), by comparing cross sections of the amplitude and phase of the three matrices $\hat{A}$, $\hat{L}$ and $\hat{U}$ for two cases: First case (cases A and C in FIG. 3(a)) - $|\alpha_s| = 0.3|\alpha_s^{Max}|$, $arg(\alpha_s) = 0.07\pi$ and $\lambda = 1440\ nm$. Second case (cases B and D in FIG. 3 (a)) - $|\alpha_s| = |\alpha_s^{Max}|$, $arg(\alpha_s) = 0.5\pi$ and $\lambda = 1000\ nm$. The comparison is for a chain with $N = 50$ particles. Very good agreement for both cases is seen. In FIG. S2(c) and FIG. S2(d) we present the associated particles' dipole moments for $\theta = 0^o$ (cases C and D in FIG. 3(a)) solved based on the derived model (solid lines) vs the exact solution (dashed lines). Also here, both cases show excellent agreement between the model and the exact solution. The cases shown in FIG. S2 correspond to $\zeta = 0.05 \cdot e^{0.19i\pi}$ (off resonance) and $\zeta = 0.37 \cdot e^{0.58i\pi}$ (on resonance).

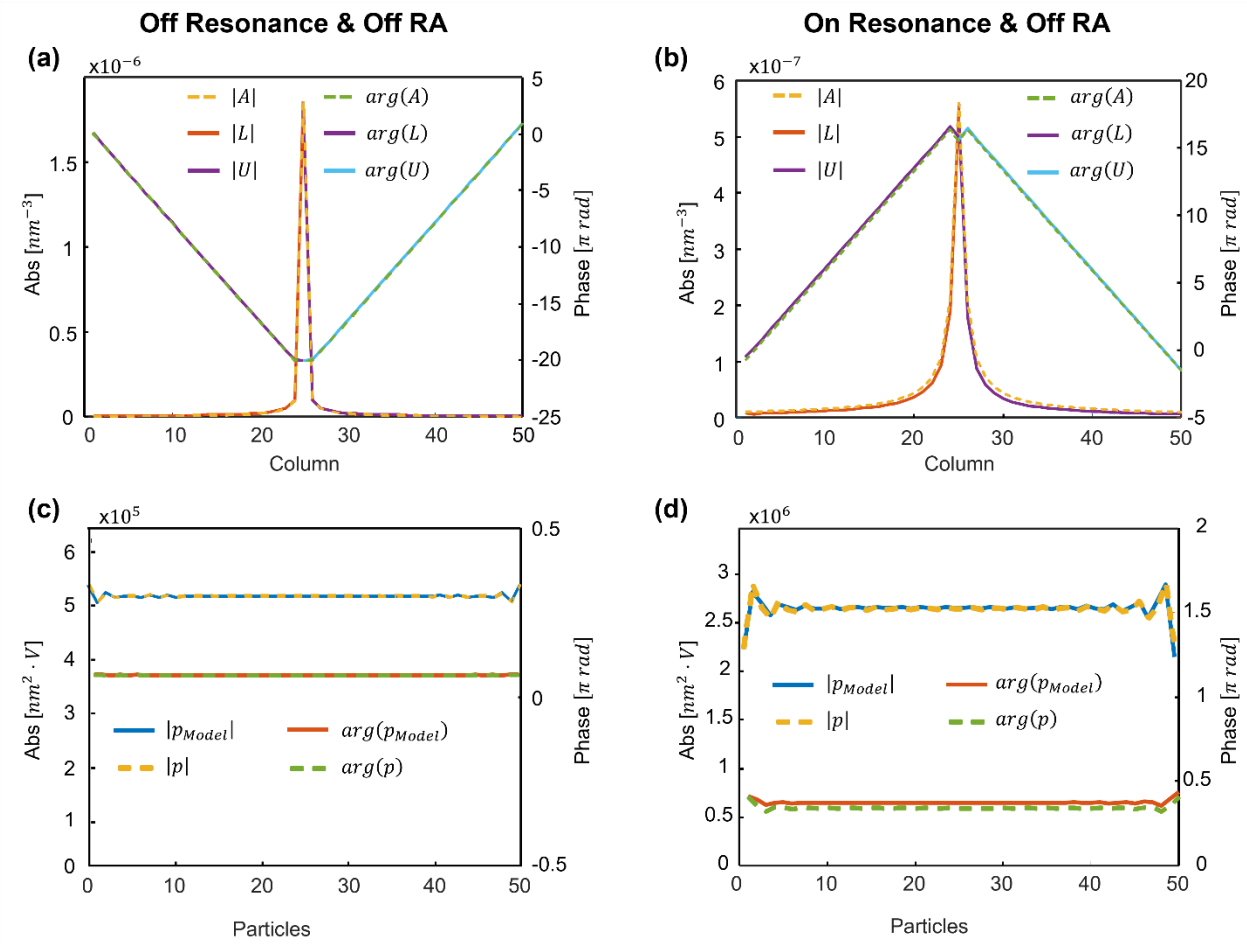

FIG. S2 Agreement of the model and the exact solution. Comparison of the amplitude and phase of the matrices L and U vs matrix A, for the case of off- (a) and on- resonance (b), both far from a RA. These correspond to cases and C and D and cases A and B in FIG. 3(a), respectively. The comparison is for the middle (25th) row. The associated particles' dipole moments solved based on the derived model for $\theta = 0^o$ (solid lines) vs the exact solution (dashed lines) is shown in (c) and (d), correspondingly (cases C and D in FIG. 3(a)). The parameters of the two cases are: Off resonance - $|\alpha_s| = 0.3|\alpha_s^{Max}|, arg(\alpha_s) = 0.07\pi, \lambda = 1440\ nm$, and on-resonance - $|\alpha_s| = |\alpha_s^{Max}|, arg(\alpha_s) = 0.5\pi, \lambda = 1000\ nm$. The comparison is for a 50-particle chain with spacing $d = 420\ nm$ and surrounding refractive index $n = 1.5$.

3. The Number of Scattering Paths as a Function of the Number of Particles

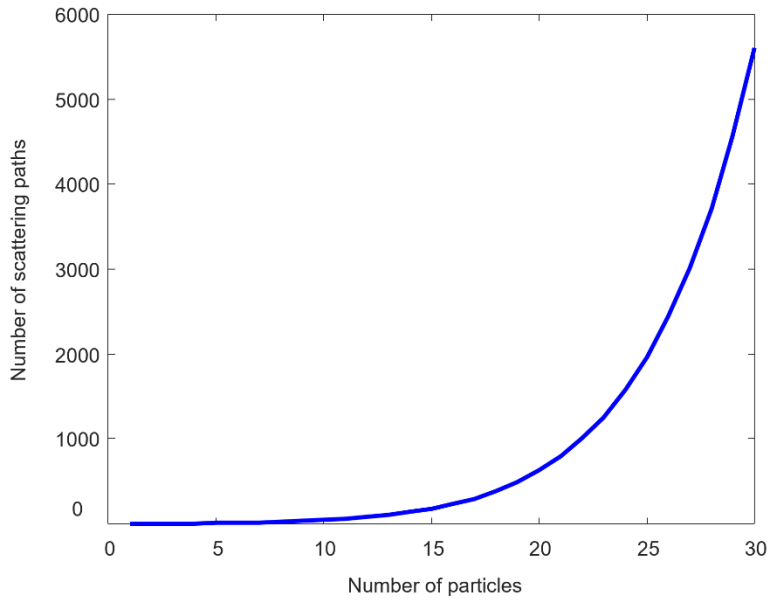

FIG. S3 Number of scattering paths as a function of the number of particles.

4. An Example of a Particle that Supports the Studied Polarizability: A Gold Nanorod

In the main text, we kept the discussion general by referring to the fundamental property that determines the optical response, i.e., the polarizability, but we noted that the values we analyze can be realized both with metallic and dielectric nanoparticles, as they rely on energy conservation considerations of the dipole mode. Here, we give an example of an actual morphology and material that supports the studied polarizability based on finite difference time domain simulations (Lumerical). The simulations were performed by extracting the absorption and scattering cross sections of the particle, and then solving from it the particle's complex polarizability.

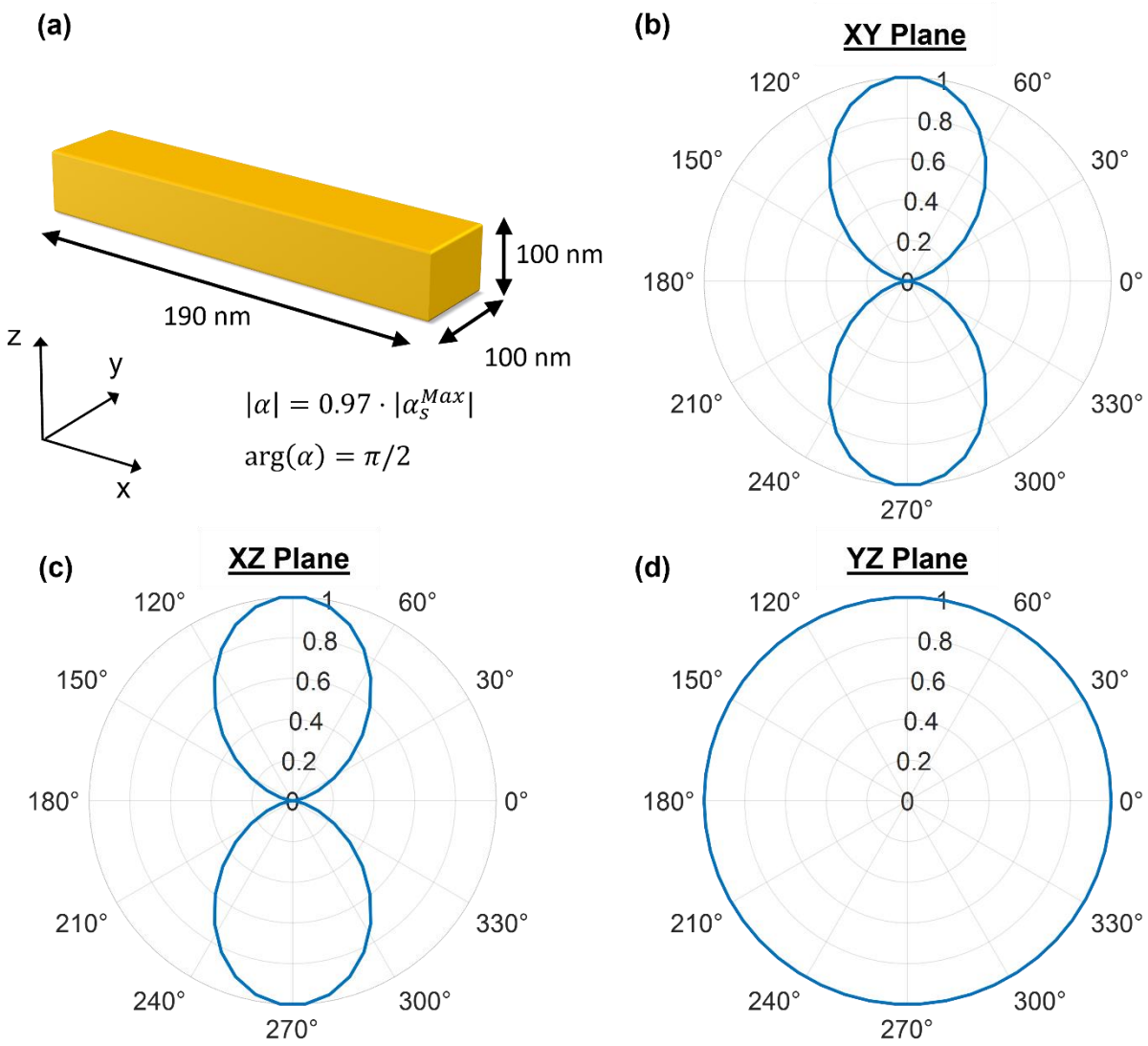

FIG. S4 An example of a nanoparticle that supports the studied polarizability. (a) An illustration of a gold nanorod with dimensions of 190 nm × 100 nm × 100 nm, that for $\lambda = 1000$ nm has a polarizability amplitude of 97% of the maximal polarizability of a single mode, $\frac{3}{2k^3}$ (Eq. 28), and a phase of $\pi/2$. The far-field radiation patterns of the rod at $\lambda = 1000$ nm in the (b) XY plane (c) XZ plane and (d) YZ plane. The radiation patterns correspond to a dipole mode excited along the x direction.

5. Wavelength Dependent Polarizability

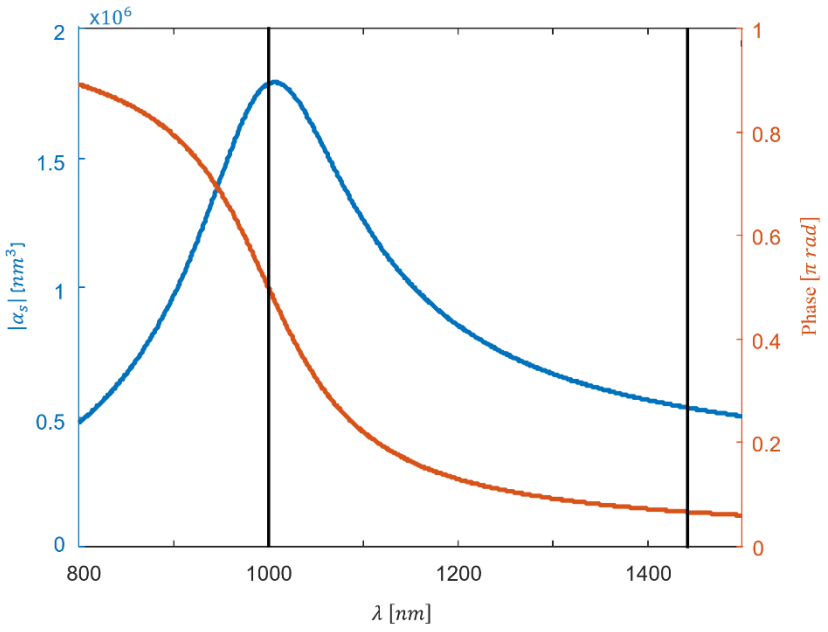

FIG. S5 Wavelength dependent polarizability. (a) The amplitude (blue) and phase (orange) of the studied nanoparticle polarizability. The black vertical lines denote the wavelengths in which the chain dynamics is explored.

6. The Diffraction Pattern of the Studied Chain

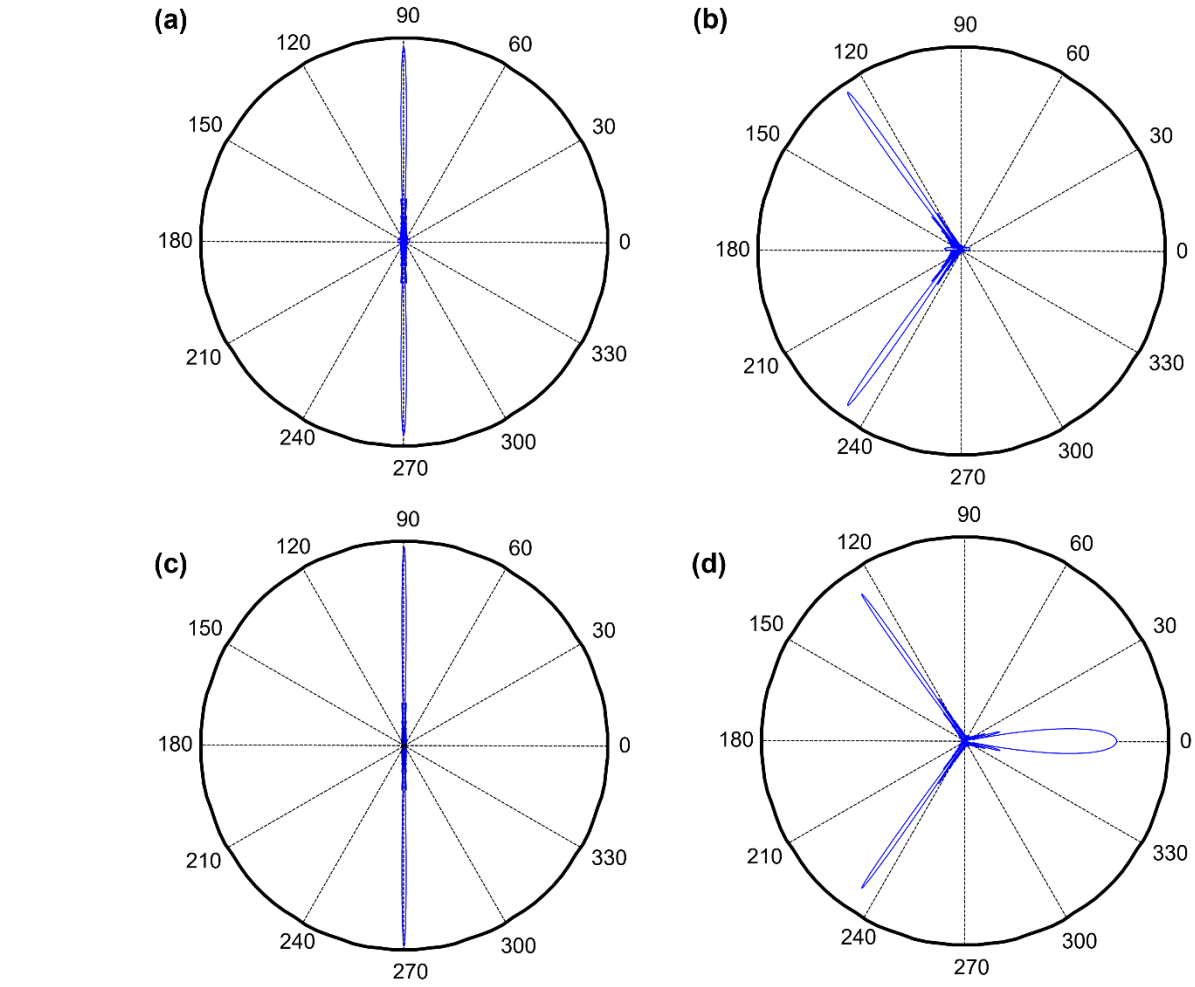

FIG. S6 The scattered fields in the YZ plane associated with the 4 cases shown in FIG. 3(a): (a) case C, (b) case A (c) case D, (d) case B. The chain is oriented along the Y direction (horizontal axis in the figures).

7. RA Induced Phase Gradient in Longer Chains

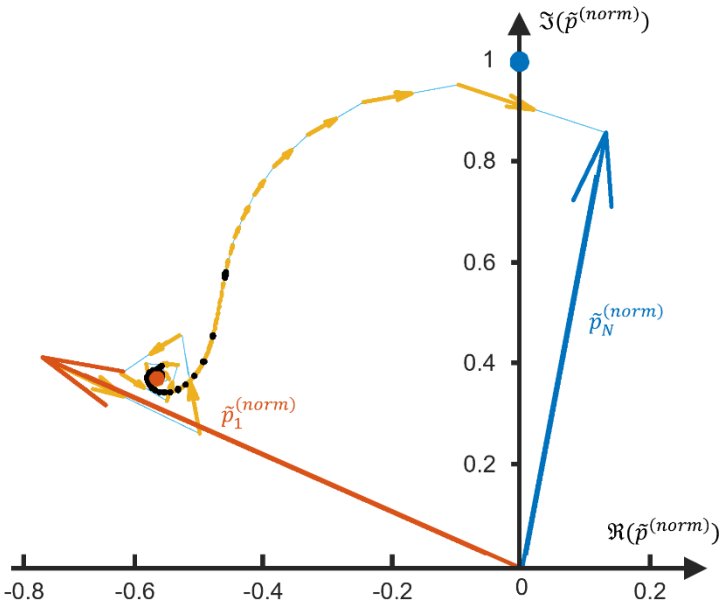

FIG. S7 RA induced phase gradient in a longer chain. The figure represents the complex plane trajectory for a chain with the same parameters as for case B in FIG. 3(a), for the case of $N = 500$ particles. The same trend as for $N = 50$ can be seen, were in the presented case the additional particles added mostly to the spiral at the beginning of the chain. In that regime, the particles roughly respond like they were in an infinite chain. This can be seen by the density of the black arrows (which appear every 10 particles) in the spiral regime vs the monotonic trajectory regime. Thus, the monotonic trajectory regime, where the coherent scattering gradually builds up, occupies a smaller portion of the chain as N increases. This results in a smaller angular deviation with respect to the FWHM of the reflected beam, as can be seen in FIG. 4 of the main text.

8. Understanding the Phase Gradients from the Dependence of B_q on q

Here we show how the mechanism that gives rise to the RA induced phase gradients becomes transparent from the phase gradient imprinted on b_q as a function of q. This gradient origins from the phase of α_s at its resonance, which is cascaded from the chain's edge. To show this, we present the evolution of b_q as a function of q in FIG. S8. First, in FIG. S8(a) we depict the phase of b_q for the off- (cases C and A in FIG. 3(a)) and on- (cases D and B in FIG. 3(a)) resonance cases. In the off-resonance case the phase varies over a small range of less than $0.2\,\pi$, where the phase saturates very rapidly (after ~5 particles). This phase trend can be understood from FIG. 5(c), which shows how the different scattering paths add up with almost the same phase. On the other hand, in the on-resonance case, a monotonic phase trend is apparent, spanning more than π phase range. In addition, the phase gradient range extends over significantly more particles than in the off-resonance case. To understand the origin of this phase gradient in b_q it is instructive to refer to the derivation according to the generalized Fibonacci series (section II-C). Figure S8(b) depicts the evolution of b_q for the on-resonance case on the complex plane. The blue points represent b_q for different q values. The yellow arrows, with the light blue guiding lines that connect the blue points, represent the difference in b_q. To see how the b_q are recursively generated we can rearrange Eqs. (17) and (20), to write:

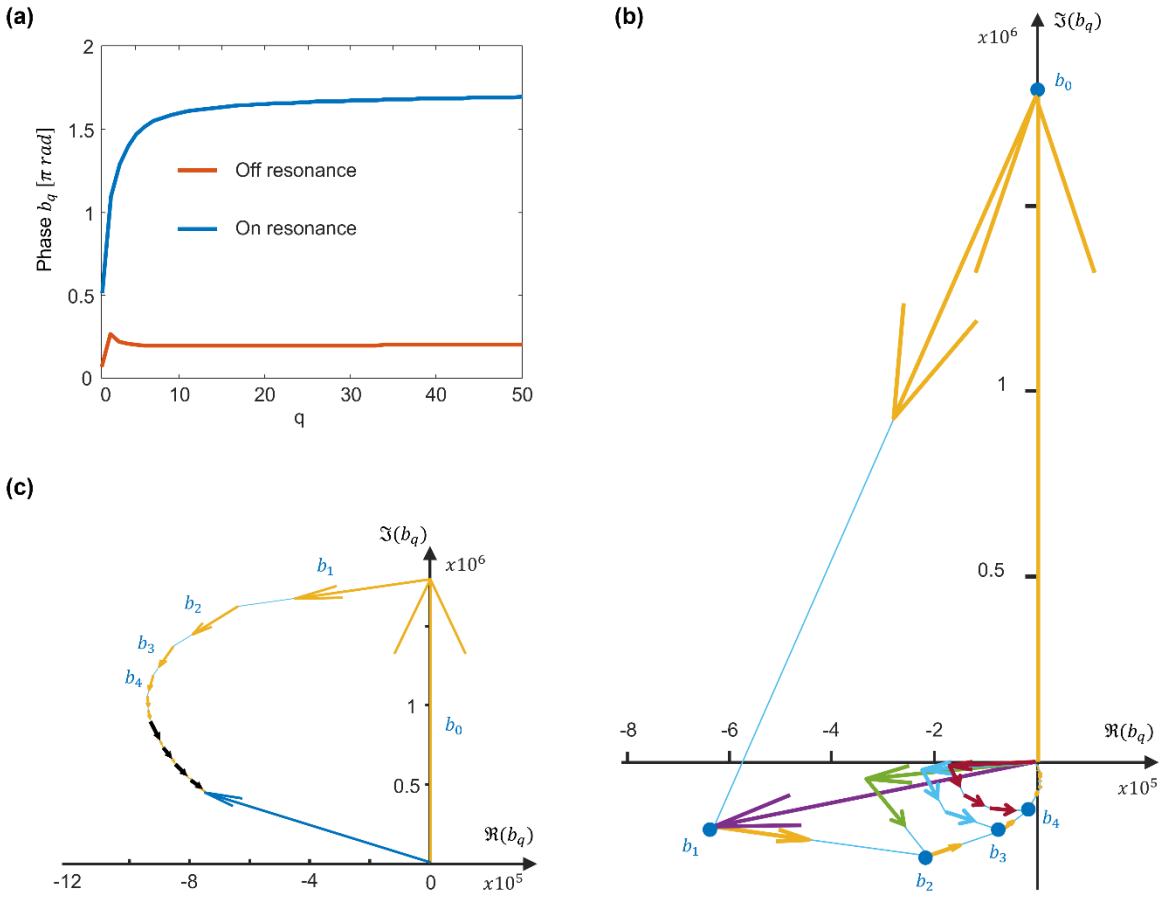

FIG. S8 The dependence of b_q on q. (a) The phase of b_q for the off- (cases C and A in FIG. 3(A)) and on- (cases D and B in FIG. 3(A)) resonance cases. In the off-resonance case the phase varies over a small range of less than 0.2π and saturates very rapidly (after ~5 particles). On the other hand, in the on-resonance case a monotonic phase trend is apparent, spanning more than π phase range. In addition, the phase gradient range extends over significantly more particles than in the off-resonance case. (b) The evolution of b_q for the on-resonance case on the complex plane. The blue points represent b_q for different q values. The yellow arrows, with the light blue guiding lines that connect the blue points, represent the difference in b_q. The arrows in purple, green, blue and dark red represent the components of the sum in Eq. (S6) for b_1, b_2, b_3 and b_4, respectively. All the different trajectories are curving counterclockwise, according to the positive phase of α_s. (c) The trajectory of the accumulative sum of the b_q terms. Each yellow arrow, along with its guiding light blue line, correspond to a certain b_q. In addition, every tenth arrow is marked in black ($q = 10, 20, 30, 40$). This trajectory has similar characteristics to the trajectory of $\tilde{p}_q$ from FIG. 4(d).

$$b_q = \sum_{i=1}^{q} w_i b_{q-i} \tag{S6}$$

In FIG. S8(b), we show in purple, green, blue and dark red arrows the components of the sum according to Eq. (S6) for b_1, b_2, b_3 and b_4, respectively. All the different trajectories are curving counterclockwise, according to the positive phase of α_s. Importantly, the recursive relation dictates that the initial phase of b_0 (α_s) will be cascaded onward, which results with a monotonic phase trend. In addition, the first component in the sum ($b_0 w_q$), which corresponds to the direct scattering, has the largest contribution for all q values. Nevertheless, the monotonic phase gradients are attributed to the non-negligible contribution of the remaining sum components. To further connect the analyzed trend of b_q as function of q to the studied response of the chain excitation ($\tilde{p}_q$), we present in FIG. S8(c) the trajectory of the accumulative sum of the b_q terms. Each yellow arrow, along with its guiding light blue line, correspond to a certain b_q, as elaborated in the figure. In addition, every tenth arrow is marked in black ($q = 10, 20, 30, 40$). This trajectory has similar characteristics to the trajectory of $\tilde{p}_q$, seen in FIG. 3(c). By referring to the two-step solution in section II-B and owing to the incoherent scattering towards the right side of the chain, we can roughly approximate p_{aux} as E_{app}. Therefore, for a RA towards the left side of the chain only the second

step of the solution determines the phase gradients, and the relation $\Delta\tilde{p}_q \approx -b_{N-q}$ holds, as discussed in section II-C. Altogether, we see how the phenomenon of a RA induced phase gradients are encoded in intrinsic characteristic of the chain. The monotonic phase of the b_q terms, determines the monotonic phase of the chain excitation.

9. RA Induced Transparency

The intriguing effect of an absorption less band induced by coherent scattering has been recently explored[2–6], showing that attractive slow light features emerge along with an induced transparency. The presented multi-scattering model can be used to explore the spatial evolution of the transparent state. The extinction cross section of the chain can be calculated by summing the extinction of all the nanoparticles[7]:

$$\sigma_{ext} = 4\pi k \sum_{q=1}^{N} \frac{\Im\{E^*_{app,q} p_q\}}{\left|E_{app,q}\right|^2} \tag{S7}$$

By recalling that $E_{app,q} = E_0 e^{-ik_{||}dq}$, we can simplify this expression to:

$$\sigma_{ext} = \frac{4\pi k}{E_0} \sum_{q=1}^{N} \Im\left\{\tilde{p}_q\right\} \tag{S8}$$

Therefore, the imaginary part of $\tilde{p}_q$ for each nanoparticle is proportional to its extinction cross section. By reexamining case B in FIG. 3(c), we observe that the extinction of each nanoparticle changes substantially from one edge of the chain to the other. A similar change can also be seen between the single particle response (blue point) to the response of a nanoparticle within an infinite chain (orange point). In case that the parameters of the chain are judiciously chosen, the dipole moment trajectory on the complex plane, as shown in FIG. 3(c), may nearly reach the horizontal axis (zero imaginary part). Hence, the extinction will almost vanish. Interestingly, it means that the chain can become almost entirely transparent, though illuminated at the absorption band of the nanoparticles. The theoretical framework developed in this paper can be beneficial for analyzing effects as this, where the particles' interaction induces a substantial change in light extinction and transmission.

10. Macroscopic Description of the Chain's Dynamics

The macroscopic analysis of the chain's modes can be performed by searching for poles of $\alpha_{eff}(\beta)$, defined in Eq. (7) of the main text, analytically continued to the complex domain. β is a complex wave number, which its real part describes the wave periodicity, and its imaginary part describes the associated decay rate. The real part can also be mapped to a corresponding angle of incidence for a plane wave illumination, $\theta_{eff} = \mathrm{asin}(\Re(\beta)/k)$. The dependence of α_{eff} on β comes through the analytical continuation of $S(\beta)$, which we can write explicitly for transverse excitation as:

$$\begin{aligned} S(\beta) = \sum_{x=-\infty, x\neq 0}^{x=\infty} G_n(x) e^{-i\beta nd} &= \sum_{n=-\infty, n\neq 0}^{n=\infty} e^{-i\beta nd} e^{ik|n|d} \left[\frac{k^2}{|n|d} + \frac{ik}{(nd)^2} - \frac{1}{(|n|d)^3}\right] \\ &= \frac{k^2}{d}\left(Li_1(z_1) + Li_1(z_2)\right) + \frac{ik}{d^2}\left(Li_2(z_1) + Li_2(z_2)\right) \\ &\quad - \frac{1}{d^3}\left(Li_3(z_1) + Li_3(z_2)\right) \end{aligned} \tag{S9}$$

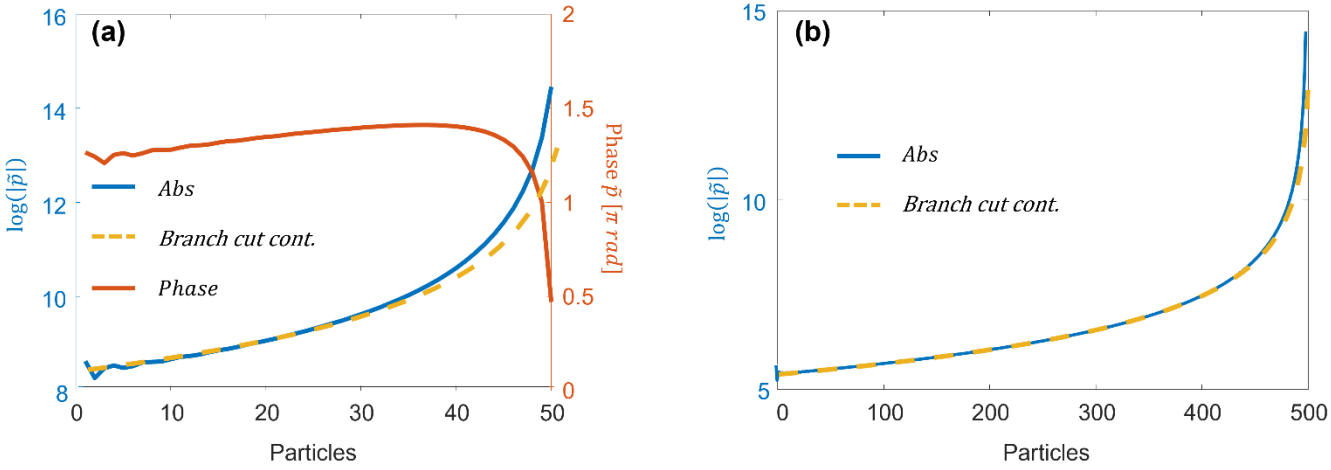

FIG. S9 Continuous spectrum wave excited at the edge of the chain for (a) 50 particles and (b) 500 particles. The figures show the dipole moments along the chain, $\tilde{p} = p/e^{ikx_n}$, for an excitation of only the last particle at the chain's edge. The amplitude (blue solid curve) agrees with the analytic expression for the branch cut contribution of the continues spectrum wave according to Eq. (S11) (yellow dashed curve). In addition, the small phase range after the subtraction of the phase associated with k (orange solid curve), confirms the existence of the continuous spectrum wave. The wavelength is $\lambda = 1000\ nm$ and the parameters of the chain are $d = 420\ nm, n = 1.5$ and $\alpha_s = \frac{3i}{2k^3}$.

Where, $z_1 = e^{id(k+\beta)}$, $z_2 = e^{id(k-\beta)}$, and $Li_s(z)$ is the s[th]-order Polylogarithm function:

$$Li_s(z) = \sum_{n=1}^{n=\infty} \frac{z^n}{n^s} \tag{S10}$$

And the analytical continuation for $|z| > 1$ is defined by $Li_0(z) = z/(1-z)$, $Li_1(z) = -ln(1-z)$ and $Li_{s+1}(z) = \int_0^z \frac{Li_s(t)}{t} dt$.

For $\lambda = 1000\ nm$ and the parameters of the analyzed chain ($d = 420\ nm, n = 1.5, \alpha_s(\lambda = 1000\ nm) = \frac{3i}{2k^3}$) we find a pole of $\alpha_{eff}(\beta)$ at $\beta = (7.4 - 1.8i)\mu m^{-1}$, which corresponds to $\theta_{eff} = 52.5°$ and a decay (of $1/e$) within a distance of $1/(\Im(\beta)d) = 1.28$ particles[1]. This angle and short interaction length confirms that neither a leaky-wave, nor a light-line mode are responsible for the observed behavior. On the other hand, the Polylogarithm function $Li_s(z)$ has a branch cut singularity which starts from the branch point $z = 0$, and extends to infinity on the real axis. This branch points occurs exactly at the RA condition and supports the resonant excitation of a continuous spectrum wave on finite chains. In our case, the resonant response of the nanoparticles stimulates the resonant excitation of the continuous spectrum wave, which decays over a long distance along the chain length. To confirm the existence of the discussed wave phenomenon we examine, in FIG. S9, the chain's response for an excitation of only a single particle at its edge. The continuous spectrum wave is expected to be excited and match a periodicity according to k (wavenumber in the medium surrounding the linear chain), with an asymptotic decay (for large number of particles) of the form[8]:

$$G_n^{cw} = \frac{d}{k^2} \frac{e^{i|n|kd}}{|n|} \prod_{m=1}^{2} \frac{1}{\ln|n| + A_m} \tag{S11}$$

where n is the particle numeration from the excited edge, $A_{1,2} = C \pm i\pi$, $C = -\frac{kd}{\alpha_s} + Li_1(e^{2ikd}) + \frac{i}{kd}\left(Li_2(e^{2ikd}) + \frac{\pi^2}{6}\right) - \frac{1}{(kd)^2}\left(Li_3(e^{2ikd}) + \zeta(3)\right)$ and $\zeta(3)$ is the Riemann zeta function of 3. Eq. (S11) accounts only for the branch cut contribution of the chain's response. In FIG. S9, we show the dipole moment excitations on a logarithmic scale (blue solid line) for a chain of 50 particles (a) and 500 particles (b). First, the nonlinear trend of the curve confirms again that neither a leaky-wave nor a light-line mode are dominant in the observed trend. In addition, the dashed yellow curve shows the function G_n^{cw} according to Eq. (S11). Very good agreement is seen as n gets larger, as expected for asymptotic approximation. The slight deviations at the end of the chain are associated with reflections from the chain's edge. Additionally, we show the phase of the dipole

[1] We note that this pole exists in the zeroth Riemann sheet for the Polylogarithm functions that depend on z_1 and in the first Riemann sheet for those who depend on z_2.

moments, where we have subtracted the phase associated with k: $\tilde{p} = p/e^{ikx_n}$. We see that the wave periodicity agrees with the wavenumber k. Overall, we see the connection between the microscopic analysis for the origin of the RA-induced phase gradient, to the macroscopic description, which reveals excitation of a continuous spectrum wave.

11. Calculation of the Power of the Diffracted Beams

The calculation of the angle-dependent normalized power of the diffracted beams is performed according to:

$$P^{(norm)}(\theta_{scat}) = \frac{|E(\theta_{scat})|^2}{P_0}$$
$$P_0 = Max(|E(\theta_{scat})|^2) \quad \text{(S12)}$$
$$E(\theta_{scat}) = \sum_{q=1}^{N} G(|\vec{r}_q - \vec{r}_{scat}|)p_q$$

Where the sum runs over the particles of the chain and $\vec{r}_{scat}$ is set to be in the far-field, pointing to the direction of the specified angle θ_{scat}. For FIG. 4(b) in the main text, the maximum in Eq. (S12) was taken to be according to the range of $\Delta\theta$ in the figure.

12. Persistence of the Angular Deviation with Varying Degree of the Radiative Loss Rate

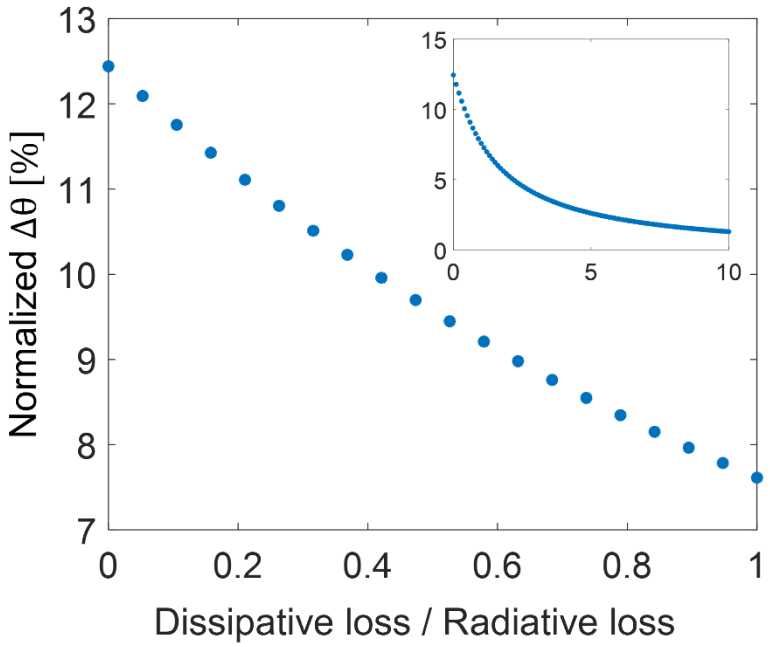

FIG. S10 The maximal angular deviation around the RA normalized to the associated FWHM as a function of the dissipative loss rate for a 50-particle chain. The angular deviation decreases as the dissipative loss rate increases. Specifically, for the critical value of dissipative loss rate that maximizes the absorption, i.e., when it equals to the radiative loss rate, the angular deviation decreases by a factor of less than two, from 12.5% to 7.6%. The inset shows the angular deviation trend beyond that point, for larger values the dissipative loss rate.

References

(1) Deif, A. Perturbation of Linear Equations. *Sensitivity Analysis in Linear Systems* **1986**, 1–43. https://doi.org/10.1007/978-3-642-82739-6_1.

(2) Michaeli, L.; Suchowski, H.; Ellenbogen, T. Near-Infrared Tunable Surface Lattice Induced Transparency in a Plasmonic Metasurface. *Laser Photon Rev* **2020**, *14* (1), 1900204. https://doi.org/10.1002/lpor.201900204.

(3) Rodriguez, S. R. K.; Janssen, O. T. A.; Lozano, G.; Omari, A.; Hens, Z.; Rivas, J. G. Near-Field Resonance at Far-Field-Induced Transparency in Diffractive Arrays of Plasmonic Nanorods. *Opt Lett* **2013**, *38* (8), 1238. https://doi.org/10.1364/ol.38.001238.
(4) Manjappa, M.; Srivastava, Y. K.; Singh, R. Lattice-Induced Transparency in Planar Metamaterials. *Phys Rev B* **2016**, *94* (16), 161103. https://doi.org/10.1103/PhysRevB.94.161103.
(5) Schaafsma, M. C.; Bhattacharya, A.; Rivas, J. G.; Goez Rivas, J. Diffraction Enhanced Transparency and Slow THz Light in Periodic Arrays of Detuned and Displaced Dipoles. *ACS Photonics* **2016**, *3* (9), 1596–1603. https://doi.org/10.1021/acsphotonics.6b00121.
(6) Tan, T. C.; Srivastava, Y. K.; Manjappa, M.; Plum, E.; Singh, R. Lattice Induced Strong Coupling and Line Narrowing of Split Resonances in Metamaterials. *Appl Phys Lett* **2018**, *112* (20), 201111. https://doi.org/10.1063/1.5026649.
(7) Hao, E.; Li, S.; Bailey, R. C.; Zou, S.; Schatz, G. C.; Hupp, J. T. Optical Properties of Metal Nanoshells. *Journal of Physical Chemistry B* **2004**, *108* (4), 1224–1229. https://doi.org/10.1021/jp036301n.
(8) Hadad, Y.; Steinberg, B. Z. Green's Function Theory for Infinite and Semi-Infinite Particle Chains. *Phys Rev B Condens Matter Mater Phys* **2011**, *84* (12), 125402. https://doi.org/10.1103/PhysRevB.84.125402.